Classification: BIOLOGICAL SCIENCES, Cell Biology

Myosin-dependent endoplasmic reticulum motility and F-actin organization in plant cells

Haruko Ueda[a], Etsuo Yokota[b], Natsumaro Kutsuna[c,d], Tomoo Shimada[a], Kentaro Tamura[a], Teruo Shimmen[b], Seiichiro Hasezawa[c,d], Valerian V. Dolja[e], and Ikuko Hara-Nishimura[a,1]

[a]Department of Botany, Graduate School of Science, Kyoto University, Kyoto 606-8502, Japan
[b]Department of Life Science, Graduate School of Life Science, University of Hyogo, Harima Science Park City, Hyogo 678-1297, Japan
[c]Department of Integrated Biosciences, Graduate School of Frontier Sciences, The University of Tokyo, Kashiwanoha Kashiwa, Chiba 277-8562, Japan
[d]Institute for Bioinformatics Research and Development (BIRD), Japan Science and Technology Agency (JST), Chiyoda-ku, Tokyo102-0081, Japan
[e]Department of Botany and Plant Pathology and Center for Genome Research and Biocomputing, Oregon State University, Corvallis, OR 97331

[1]To whom correspondence should be addressed.
Ikuko Hara-Nishimura
Department of Botany, Graduate School of Science, Kyoto University, Kyoto 606-8502, Japan
Phone and fax 81-75-753-4142; E-mail ihnishi@gr.bot.kyoto-u.ac.jp.

Manuscript information: 19 text pages and 4 figures.

Key Words: myosin XI; endoplasmic reticulum; cytoplasmic streaming; actin filament; *Arabidopsis thaliana*.

Abstract

Plants exhibit an ultimate case of the intracellular motility involving rapid organelle trafficking and continuous streaming of the endoplasmic reticulum (ER). Although it was long assumed that the ER dynamics is actomyosin-driven, the responsible myosins were not identified, and the ER streaming was not characterized quantitatively. Here we developed software to generate a detailed velocity distribution map for the GFP-labeled ER. This map revealed that the ER in the most peripheral plane was relatively static, whereas the ER in the inner plane was rapidly streaming with the velocities of up to ~3.5 μm/sec. Similar patterns were observed when the cytosolic GFP was used to evaluate the cytoplasmic streaming. Using gene knockouts, we demonstrate that the ER dynamics is driven primarily by the ER-associated myosin XI-K, a member of a plant-specific myosin class XI. Furthermore, we show that the myosin XI deficiency affects organization of the ER network and orientation of the actin filament bundles. Collectively, our findings suggest a model whereby dynamic three-way interactions between ER, F-actin, and myosins determine the architecture and movement patterns of the ER strands, and cause cytosol hauling traditionally defined as cytoplasmic streaming.

Cytoplasmic streaming defined as an extensive intracellular motility in plants was first described in 1774 (1). It is thought that unidirectional actin filament (AF) bundles and organelle-associated myosins XI, a plant-specific class of myosin motors, cause bulk flow in the cell (reviewed in (2-4)). Some myosins XI were indeed reported to slide along AFs *in vitro* (5, 6). Using immunocytochemical analyses (7-11) and fluorescent protein-labeled myosins (12, 13), it was shown that myosins XI are associated with the particulate organelles. Recent analyses using gene knockouts and dominant negative inhibition demonstrated that several class XI myosins have overlapping

functions in the rapid movement of organelles (14-18). Among these, myosin XI-K was found to play the most prominent role in the movement of Golgi bodies, peroxisomes, and mitochondria. It was also concluded that none of these three organelles fits the paradigm of cytoplasmic streaming raising the question of what drives this conspicuous process (14, 15).

The endoplasmic reticulum (ER), an organelle present in all eukaryotic cells, harbors the largest reservoir of cellular membranes. Cytoskeleton-dependent remodeling of the ER network, which consists of cisternae and interconnected membrane tubes is well known in both animals and plants (reviewed in (19-22)). In addition, dynamic streaming of the plant ER has been observed in sub-peripheral cytoplasm and transvacuolar strands (23-25). However, molecular mechanism underlying the ER streaming is not known, although it was reported that the 175 kDa myosin XI was localized on the ER of tobacco cell culture BY-2 (26).

Unlike the movement of the particulate organelles, quantitative analysis of the ER streaming was long hampered by the inherent difficulty of ER tracking. Here, we measured the ER streaming using newly developed software, and identified an *Arabidopsis* myosin XI-K as the primary contributor to ER streaming. We have also implicated class XI myosins into the organization of the AF bundles and advanced a model according to which rapid, myosin-dependent ER motility along the thick AF bundles is a driver of cytoplasmic streaming.

Results and Discussion

Quantitative Analyses of the ER Movement and Cytoplasmic Streaming. We used the epidermal cells of cotyledonary petioles of the transgenic *Arabidopsis* expressing ER-localized GFP (GFP-h) as a convenient model to follow the ER dynamics. In these cells, we observed a relatively static peripheral ER network and the rapidly moving thick strands with high GFP fluorescent intensities, which we

designated as ER strands (Fig. 1*A*, and Movies S1 and S2). The ER strands streamed mostly along the longitudinal axis of the cell (Movies S1 and S2).

To comprehensively analyze the ER movement, we developed a software, KbiFlow plugin package for ImageJ software, based on the optical flow analysis. KbiFlow generates a velocity map by calculating the average velocity of 16 x 16 pixels (2.54 μm x 2.54 μm) in 100 time-lapse images for ~5.4 sec (Fig. S1) and makes it possible to estimate not only the velocity and the direction, but also the distribution of the streaming in a wide field. The velocity maps showed that the ER is composed of several regions that move in distinct orientations and with variable velocities within a focal plane (Fig. S2). The velocity maps highlighted the rapidly moving thick ER strands.

For each analyzed cell, we selected two ~1-μm-thick optical planes at ~1.5 μm distance, a peripheral plane and an interior plane, and calculated maximum and average ER velocities in each plane. Statistical analysis of 16 cells showed that the maximal ER velocities were 1.35 μm/sec for the cell periphery and 2.20 μm/sec for the cell interior ($P < 0.005$ by Mann-Whitney test), whereas the average velocities were 0.33 μm/sec and 0.48 μm/sec for the cell periphery and interior, respectively ($P < 0.05$ by Mann-Whitney test) (Fig. S2*E* and Table S1). This analysis showed that the ER in the peripheral plane was relatively static (Movie S1), whereas the ER in the inner plane was rapidly streaming (Movie S2).

To obtain an insight into the dynamics of cytosol per se, we used transgenic expression of a cytosolic form of GFP reporter. Interestingly, the streaming pattern of cytosolic GFP was similar to that of the ER-localized GFP (compare Movies S2 and S3, and Figs. S2 and S3). More specifically, the velocity map of cytosolic GFP also showed substantial degree of local variation (Fig. S3 *C* and *D*). By the KbiFlow analysis of 22 cells, maximal velocities for a peripheral and an interior planes were 1.23 and 1.99 μm/sec ($P < 0.0005$ by Mann-Whitney test), and average velocities were 0.37 and 0.49 μm/sec ($P < 0.005$ by Mann-Whitney test), respectively (Table

S1). These velocities were comparable to those of ER streaming in each focal plane (Table S1). Although the brightness of cytosolic GFP is a subject for multiple processes such as local expression level, cytosol stirring, and mere thermal diffusion, so far, cytosolic GFP provides the best approximation for a measure of cytoplasmic streaming. Therefore, these data suggest a correlation and a causative relationship between the streaming of ER and cytosol.

Myosin XI-K Is the Primary Contributor to ER Streaming. The ER dynamics was dose-dependently inhibited by the treatments with either latrunculin B (Lat B), an inhibitor of actin polymerization, or 2,3-butanedione monoxime (BDM), an inhibitor of myosin activity (Fig. S4 and Movies S4 and S5). Another inhibitor of actin polymerization, cytochalasin B, was also reported to inhibit the ER movement in onion epidermal cells (24). Taken together, these results suggested that the ER streaming requires both the active myosin motors and the intact actin cytoskeleton. To identify the myosins responsible for ER streaming, we analyzed gene knockout mutants in which three class XI myosins, XI-K, MYA1/XI-1, and MYA2/XI-2, that are ubiquitously expressed throughout the plants (http://atted.jp) (27, 28) were inactivated (Fig. S5).

Among the eight tested independent insertion mutant alleles (*mya1-1, mya1-2, mya2-1, mya2-2, xik-1, xik-2, xik-3* and *xik-4*; Fig. S5*A*), ER streaming was dramatically suppressed only in those targeting myosin XI-K gene (Movie S6 for *xik-2*). The velocity maps of the ER streaming in *xik-1* and *xik-2* mutants showed obvious reductions in the number of bright arrows that represent high velocity streaming (Figs. 1 *H* and *I*) compared to that in the GFP-h map (Fig. 1*G*). The maximal and average ER velocities in each of the *xik-1* and *xik-2* mutants were only ~35% and ~50%, respectively, of those in GFP-h (Fig. 1*M* and Table S1).

We further obtained a series of five homozygous double and triple knockout mutants of the myosins XI-K, MYA1/XI-1, and MYA2/XI-2: *mya1 mya2* (*mya1-1*

mya2-2), *xik mya1* (*xik-2 mya1-1*), *xik mya2* (*xik-2 mya2-2*), and *xik mya1 mya2* (*xik-2 mya1-1 mya2-2* and *xik-1 mya1-2 mya2-1*). Among these mutants, the two triple mutants showed the strongest suppression of ER streaming (Fig. 1 and Movie S7). The average ER velocities in the triple mutants were ~30% of that in GFP-h, whereas the corresponding maximal velocities were reduced to less than ~20% (Fig. 1*M* and Table S1). On the other hand, ER streaming was slightly suppressed in the *mya1 mya2* double gene knockout, but not in the *mya1* or *mya2* single gene knockout mutants (Fig. 1*M* and Fig. S6). These results indicate that the myosin XI-K is the primary contributor to ER streaming, whereas the contributions of the myosins MYA1/XI-1 and MYA2/XI-2 are more limited.

In-vitro motility assays have shown that the recombinant motor head of MYA1/XI-1, which is the most closely related myosin XI-K paralog, is able to translocate F-actin with a velocity of 3.2 μm/sec (29). The velocity of ER streaming measured here is up to 3.5 μm/sec (Fig. S2*E*), indicating that the myosin translocation velocities assayed *in vitro* and *in vivo* are similar.

Association of Myosin XI-K with ER. To determine if myosin XI-K is physically associated with ER, we generated a transgenic *Arabidopsis* line that constitutively expressed GFP fused with the C-terminal region of the myosin XI-K (GFP-XIKct) which harbored both a dimerization coiled-coil domain and a globular, cargo-binding, tail domain (30). Our attempts to use the GFP-XIKct reporter for direct microscopic observation of a potential association with ER were hampered by the strong fluorescence of the cytosolic pool of GFP-XIKct also observed by others (12, 17, 18). Because of that, we used subcellular fractionation as the means to separate ER from other cell components and to test for the presence of myosin XI-K in the ER-enriched fractions using antibodies specific to *Arabidopsis* myosin XI-K (14).

Sucrose density gradient centrifugation of a microsomal fraction was performed in the presence of either $MgCl_2$ or EDTA to follow the shift in ER migration due to the

release of ribosomes under EDTA treatment. It was found that the myosin XI-K peaked in the same gradient fractions as the ER marker BiP in the absence of Mg^{2+} (Fig. 2*A*). Furthermore, both myosin XI-K and BiP showed identical Mg^{2+}-dependent density shift in the gradients (Fig. 2*B*). These results demonstrated that a substantial fraction of the cellular pool of myosin XI-K co-migrates with ER in the density gradients in a Mg^{2+}-dependent manner, and therefore is likely associated with ER.

On the other hand, there was no correspondence between the gradient peaks of the Golgi marker RGP1 and myosin XI-K (Fig. 2); an unexpected result given that the myosin XI-K inactivation suppresses the movements of Golgi bodies (14, 15). Because Golgi bodies are physically attached to the ER tubes (31) as is also obvious from the presence of Golgi marker in the peak ER fractions (Fig. 2), it seems possible that most of the myosin XI-K-containing Golgi bodies co-migrate with the ER in gradients. Alternatively, because the overall surface of the ER is overwhelmingly larger than that of Golgi, the immunocytochemical signal from the ER-associated myosin is also much stronger than that from Golgi.

Myosin XI-K Is Involved in Maintaining Spatial Configuration of the ER. As seen in Fig. 1, inactivation of the myosin XI-K affected not only the ER movement but also the formation of thick, highly mobile ER strands, suggesting that myosin XI-K is required for the proper spatial configuration of the ER. More detailed analysis of the ER network revealed defects in the development of the transvacuolar cytoplasmic strands formed by the AF bundles in the *xik* knockout mutants (Fig. 3 *A*-*C*). This result is consistent with the previous reports of the reduced number of transvacuolar strands upon BDM treatment (32, 33). Additionally, multiple myosin knockout mutants had unevenly distributed thick-sheet-like structures of the ER network (Fig. 3*E*) and large ER aggregates mainly at the cell edges (Fig. 3 *F* and *G* and Movie S8, discussed below). These abnormal ER configurations were most evident in the *xik mya1 mya2* triple knockout, whereas double knockout *mya1 mya2* had no obvious

abnormality (Fig. S6*D*).

In addition to regular ER network, *Arabidopsis* cells possess ER-derived spindle-shaped organelles, called ER bodies, which are observed to stream in the cortical region and transvacuolar strands of the epidermal cells of the seedlings (Fig. S7 *A*-*C*). The ER bodies in *xik mya1 mya2* triple knockout exhibited abnormally elongated shapes and distribution often accumulating as concatemers in a perinuclear region (Fig. 3*G;* Fig. S7 *D*-*F*). Double knockout mutants *xik mya2* and *xik mya1* showed a milder phenotype than the triple mutant. Taken together, these results suggest that the ER-associated myosin XI-K is involved in maintaining the proper ER organization and determining the size and distribution of the ER bodies by driving the ER streaming.

Reorganization of the Actin Filament Bundles in Myosin XI-K–Deficient Mutants. In accord with the known role of the actin cytoskeleton in ER network organization (34), we have observed the abnormal ER configuration in the wild-type cells treated with Lat B to disassemble AFs (Fig. S4 *B*-*D*). To further examine the relationships between the ER network and the actin cytoskeleton in the myosin-deficient plants, we generated transgenic lines that expressed both the ER-localized GFP and the F-actin marker tdTomato-ABD2 based on the improved variant of the red fluorescent protein (35, 36).

The epidermal cells of cotyledonary petioles in the Columbia-0 (Col-0) background exhibited thick, longitudinally oriented AF bundles, with the ER streaming occurring along these bundles (Fig. 4*A*). Strikingly, the AF bundles were randomly oriented in a double myosin knockout *xik mya2*, whereas the typical ER strands were mostly absent (Fig. 4*B*). The double mutant also exhibited abnormal distributions of the ER (the thick-sheet-like structures and large aggregates of the ER) as did the triple mutant *xik mya1 mya2* (Fig. 3 *E*-*G*). Collectively, these results suggest that the ER strand formation involves myosin XI-dependent, dynamic bridging of the ER

subdomains, such as tubules and amorphous cisternae, to AF. Rapid, directional transport of these subdomains results in their orientation and concentration along the AF bundles, producing motile, brightly fluorescent, ER strands.

We quantitatively analyzed the orientation of the AF-bundles labeled with tdTomato-ABD2 by image processing (Fig. S8*A*). Statistical analysis of 20~24 cells showed that the average angle of the AFs against longitudinal axis of the cell in *xik mya2* was larger than that in Col-0 ($P < 0.05$ by Student's *t*-test), whereas the parallelness of AFs in *xik mya2* was lower than that in Col-0 ($P < 0.001$ by Student's *t*-test) (Fig. 4*C*). In order to exclude the possibility that the organization of AF bundles was affected by the overexpression of tdTomato-ABD2 reporter, endogenous AFs in the nontransgenic plants were observed by Alexa 546–phalloidin staining (Fig. S9). In the double and triple knockouts *xik mya2* and *xik-2 mya1-1 mya2-2*, the AF bundles again showed random distribution with some bundles oriented perpendicularly to the longitudinal direction of the cell (Fig. S9 *G*, *H*, *J*, and *K*). In contrast, this pattern was rarely observed in the Col-0, *mya1*, *mya2*, *mya1 mya2*, *xik*, and *xik mya1* backgrounds (Fig. S9 *A*-*F* and *I*). Myosin XI-K deficiency had a significant effect on ER motility (Fig. 1), but did not noticeably alter actin organization.

Similar phenomena were revealed in the epidermal cells of the etiolated hypocotyls. Col-0 hypocotyls had thick, longitudinally oriented AF bundles, with the ER streaming occurring along these bundles (Fig. S8 *B* and *D*, Movie S9), while *xik mya2* hypocotyls, which had randomly oriented AF bundles, exhibited neither ER strands nor streaming (Fig. S8 *C* and *D*, Movie S10).

These results indicated that the myosins XI-K and MYA2/XI-2 are collectively required for the maintenance of the thick AF bundles and associated ER strands, at least in the certain types of the elongated cells. As recently proposed by Staiger et al. (37), plant myosins could play a role in the constant buckling and straightening of AFs. Our data provide experimental evidence supporting the emerging concept of the myosin-dependent AF dynamics required for the formation and positioning of the AF

bundles.

Conclusions. Our findings provide novel insight into the mechanisms of the actomyosin-driven intracellular motility in higher plants. We find that the myosin XI-K is associated with ER and acts as the primary contributor to the ER streaming. We further show that the myosin XI-K in cooperation with the myosin MYA2/XI-2 is involved in organizing AF bundles and the associated ER strands. To address the significance and the outcome of the three-way interactions among ER, AFs, and myosins, we propose a following model involving a positive-feedback loop. Initially, the myosin-associated ER sub-domains slide along randomly oriented actin filaments (or immature AF bundles). Such ER sliding gradually promotes formation of the unidirectionally-oriented, thick AF bundles by aligning the adjacent AF bundles through the ER-associated myosins. Reiteration of this process in the elongated cells results in a formation of a few, longitudinally oriented, thick AF bundles that provide tracks for the extensive streaming of the ER strands. Because the ER network is the largest cellular endomembrane system, it seems to be a natural candidate for the anchoring and aligning multiple AFs throughout the elongated cells. Furthermore, the large mass and surface area of the unidirectionally streaming ER is likely to haul the cytosol along resulting in a concomitant passive cytoplasmic streaming. Our results showing similar patterns and velocities of the ER and cytosol streaming are well compatible with this concept.

Materials and Methods

Plant Materials and Growth Conditions. *Arabidopsis thaliana* ecotype Col-0 was used as the wild-type plant. We used the following *Arabidopsis* transgenic lines: GFP-h (38), and the plants expressing cytosolic GFP (39). Seeds of *Arabidopsis* were surface-sterilized and then sown onto 0.5% Gellan Gum (Wako, Tokyo, Japan) which contained 1% sucrose and Murasige-Skoog's medium. After incubation for 3-5 days at 4˚C to break seed dormancy, the plants were grown at 22˚C under continuous light.

Imaging of ER Streaming. We used abaxial epidermal cells in 7-day-old cotyledonary petioles for the imaging of ER streaming.

We analyzed two ~1-μm-thick optical planes at ~1.5 μm distance, a peripheral plane and an interior plane, for Figs. S2 and S3 and a sub-peripheral focal plane located between these planes for Figs. 1, S4, and S6. The ER streaming was observed with a fluorescence microscope (Axioplan 2 Imaging, Carl Zeiss, Jena, Germany) equipped with a confocal laser scanning unit (CSU 10, Yokogawa Electric, Tokyo, Japan) and the laser unit (Sapphire 488 Coherent, CA). We collected the time-lapse images of ER by an EM-CCD camera (C9100, Hamamatsu Photonics, Japan) with a 100 x 1.45 numerical aperture oil-immersion objective. For each cell, 100 frames were continuously scanned during ~5.4 s (frame rate: 50 ms / frame). ER streaming was analyzed using our in-house developed plugin package, KbiFlow, for ImageJ software (NIH; See Supplemental Information). The KBI plugin package can be downloaded for free from http://hasezawa.ib.k.u-tokyo.ac.jp/zp/Kbi/ImageJKbiPlugins.

Myosin XI-Deficient Mutants. T-DNA-tagged mutants of XI-K, MYA1/XI-1, and MYA2/XI-2 were established (Fig. S5). Double and triple mutants of myosin XI were generated by crossing single mutants. Seeds of T-DNA-tagged mutants were obtained from Salk Institute Genomic Analysis Laboratory. *mya2-1* was described

previously (10). To visualize ER in myosin XI-deficient mutants, single mutants were crossed with *GFP-h*. Alternatively, a *SP-GFP-HDEL* gene (40) was stably transformed into double and triple mutants via *Agrobacterium*.

Plasmid Construction and Transformation. DNA sequence corresponding to C-terminal tail region of XI-K (XIKct) was amplified by PCR with a cDNA library prepared from *Arabidopsis* Col-0 and KOD plus polymerase (Toyobo, Osaka, Japan). A pair of specific primers (XI-K-CT-for, 5'-caccCTTAAGATGGCCGCACGAGACACA-3'; and XI-K-CT-rev, 5'-TTACGATGTACTGCCTTCTTTACGTGT-3'). Amplified fragments were subcloned into pENTR/D-TOPO using Gateway TOPO cloning kit (Invitrogen) and sequenced. To express XIKct as a GFP-XIKct fusion protein, the *XIK* construct was introduced into pGWB406 plant expression vector by LR reaction of the Gateway system (Invitrogen) (41). The construct was introduced into *Arabidopsis* Col-0 plants by the floral dip method (42).

Subcellular Fractionation. The aerial parts of 17-day-old GFP-XIKct plants (1.5 g fresh weight) were chopped with a razor blade in a Petri dish on ice in 6 mL of 5 mM EDTA or 5 mM $MgCl_2$ and 5 mM EGTA in extraction buffer (30 mM PIPES-KOH, pH 7.0, 0.4 M sucrose, 1 mM DTT, 1 mM PMSF, 0.1 mg/mL leupeptin and 1% casein). The homogenate was filtered through a Cell Strainer (70 μm) by centrifugation at 500 rpm. An aliquot of the filtrate was used as the total fraction. The microsomal fractions were prepared by sequential centrifugations of the total fraction at 2,000 *g* for 20 min and 100,000 *g* for 1 h. The 100,000 *g* pellets were resuspended in 0.2 mL of the extraction buffer without 1% casein in the presence of 5 mM EDTA or 5 mM $MgCl_2$ and 5 mM EGTA and layered directly on top of a 16-mL linear sucrose density gradient (15 to 50%, w/w). Centrifugation was performed in an SW28.1 rotor (Beckman) at 25,000 rpm for 20 h at 4˚C, and 700-μL fractions were collected with a piston gradient fractionator (TOWA LABO). Each fraction was concentrated with acetone and subjected to SDS-PAGE and immunoblot analyses, as described

previously (43). Antibodies used were anti-XI-K (diluted 5,000-fold) (14), anti-BiP (diluted 10,000-fold) (44), and anti-RGP1 (diluted 10,000-fold) (45).

Confocal Laser Scanning Microscopy. The fluorescent images were inspected with a confocal laser scanning microscope (LSM510 META; Carl Zeiss) using the 488-nm line of a 40-mW Ar/Kr laser or the 543-nm line of a 1-mW He/Ne laser with either a 63 x 1.2 numerical aperture water-immersion objective or a 20 x 0.8 numerical aperture dry objective. The data were processed using Adobe Photoshop (Adobe Systems, Tokyo, Japan) or ImageJ.

Visualization of Actin Filaments. Actin filaments were visualized with tdTomato-ABD2 which expresses actin binding domain 2 of *Arabidopsis thaliana* Fimbrin 1 (ABD2 AtFim1) fused to tdTomato (35, 36). We introduced stably this construct into GFP-h or myosin XI mutants that expressed ER-localized GFP. Because homozygous *tdTomato-ABD2* caused delay of growth to *xik mya2*, we used the *xik mya2* plants with heterozygous *tdTomato-ABD2* in which the growth rates were similar to those in *xik mya2*. Orientation of AF-bundles was analyzed using our in-house developed plugin package, KbiLineExtract, for ImageJ software (Fig. S8*A*, see Supplemental Information).

Acknowledgments

We thank Drs. S. Mano and M. Nishimura (National Institute for Basic Biology) for donating transgenic *Arabidopsis* expressing cytosolic GFP, Drs. P. M. Ray and K. S. Dhugga (Stanford University) for providing anti-pea RGP1 antibody, Dr. T. Higaki (The University of Tokyo) for providing the *Arabidopsis ABD2 Fim1* gene in the pUC18 vector, and Dr. T. Nakagawa (Shimane University) for providing pGWB406. This work was supported by Grants-in-Aid for Scientific Research from the Ministry of Education, Culture, Sports, Science and Technology (MEXT) of Japan to I. H.-N. (nos. 16085203 and 17107002) and to H. U. (nos. 20770032 and 21200065) and by the Global Center of Excellence Program “Formation of a Strategic Base for

Biodiversity and Evolutionary Research: from Genome to Ecosystem" of MEXT. The work in V.V.D. lab is supported by NIH ARRA award (no. GM087658).

References

1. Corti B (1774) Osservazioni microscopiche sulla tremella e sulla circolazione del fluido in una pianta acquajuola. Lucca
2. Grolig F, Pierson ES (2000) in *Actin: A Dynamic Framework for Multiple Plant Cell Functions*, eds. Staiger, C. J., Baluska, F., Volkmann, D. & Barlow, P. (Kluwer Academic Publishers, Dordrecht, The Netherlands), pp. 165-190.
3. Shimmen T, Yokota E (2004) Cytoplasmic streaming in plants. *Curr Opin Cell Biol* 16:68-72.
4. Shimmen T (2007) The sliding theory of cytoplasmic streaming: fifty years of progress. *J Plant Res* 120:31-43.
5. Yokota E, et al. (1999) Biochemical and immunocytochemical characterization of two types of myosins in cultured tobacco bright yellow-2 cells. *Plant Physiol* 121:525-534.
6. Tominaga M, et al. (2003) Higher plant myosin XI moves processively on actin with 35 nm steps at high velocity. *Embo J* 22:1263-1272.
7. Yokota E, et al. (1995) Localization of a 170 kDa myosin heavy chain in plant cells. *Protoplasma* 185:178-187.
8. Liu L, Zhou J, Pesacreta TC (2001) Maize myosins: diversity, localization, and function. *Cell Motil Cytoskeleton* 48:130-148.
9. Wang Z, Pesacreta TC (2004) A subclass of myosin XI is associated with mitochondria, plastids, and the molecular chaperone subunit TCP-1alpha in maize. *Cell Motil Cytoskeleton* 57:218-232.
10. Hashimoto K, et al. (2005) Peroxisomal localization of a myosin XI isoform in Arabidopsis thaliana. *Plant Cell Physiol* 46:782-789.
11. Romagnoli S, et al. (2007) Microtubule- and actin filament-dependent motors are distributed on pollen tube mitochondria and contribute differently to their movement. *Plant Cell Physiol* 48:345-361.
12. Reisen D, Hanson MR (2007) Association of six YFP-myosin XI-tail fusions with mobile plant cell organelles. *BMC Plant Biol* 7:6.
13. Li JF, Nebenfuhr A (2007) Organelle targeting of myosin XI is mediated by two globular tail subdomains with separate cargo binding sites. *J Biol Chem* 282:20593-20602.
14. Peremyslov VV, Prokhnevsky AI, Avisar D, Dolja VV (2008) Two class XI myosins function in organelle trafficking and root hair development in Arabidopsis. *Plant Physiol* 146:1109-1116.
15. Prokhnevsky AI, Peremyslov VV, Dolja VV (2008) Overlapping functions of the four class XI myosins in Arabidopsis growth, root hair elongation, and organelle motility. *Proc Natl Acad Sci U S A* 105:19744-19749.
16. Avisar D, et al. (2008) Myosin XI-K Is required for rapid trafficking of Golgi stacks, peroxisomes, and mitochondria in leaf cells of Nicotiana benthamiana. *Plant Physiol* 146:1098-1108.
17. Sparkes IA, Teanby NA, Hawes C (2008) Truncated myosin XI tail fusions inhibit peroxisome, Golgi, and mitochondrial movement in tobacco leaf epidermal cells: a genetic tool for the next generation. *J Exp Bot* 59:2499-2512.
18. Avisar D, et al. (2009) A comparative study on the involvement of 17 Arabidopsis myosin family members on the motility of Golgi and other

organelles. *Plant Physiol* 150:700-709.
19. Lichtscheidl IK, Baluska F (2000) in *Actin: A Dynamic Framework for Multiple Plant Cell Functions*, eds. Staiger, C. J., Baluska, F., Volkmann, D. & Barlow, P. (Kluwer Academic Publishers, Dordrecht, The Netherlands), Vol. Developments in Plant and Soil Sciences, Vol. 89, pp. 191-201.
20. Voeltz GK, Rolls MM, Rapoport TA (2002) Structural organization of the endoplasmic reticulum. *EMBO Rep* 3:944-950.
21. Quader H, Zachariadis M (2006) in *The plant endoplasmic reticulum*, ed. Robinson, D. G. (Springer, Berlin / Heidelberg), Vol. Plant Cell Monographs, pp. 1-23.
22. Borgese N, Francolini M, Snapp E (2006) Endoplasmic reticulum architecture: structures in flux. *Curr Opin Cell Biol* 18:358-364.
23. Quader H, Schnepf E (1986) Endoplasmic reticulum and cytoplasmic streaming: Fluorescence microscopical observations in adaxial epidermis cells of onion bulb scales. *Protoplasma* 131:250-252.
24. Allen NS, Brown DT (1988) Dynamics of the endoplasmic reticulum in living onion epidermal cells in relation to microtubules, microfilaments, and intracellular particle movement. *Cell Motil Cytoskeleton* 10:153-163.
25. Boevink P, et al. (1996) Virus-mediated delivery of the green fluorescent protein to the endoplasmic reticulum of plant cells. *Plant J* 10:935-941.
26. Yokota E, et al. (2009) An isoform of myosin XI is responsible for the translocation of endoplasmic reticulum in tobacco cultured BY-2 cells. *J Exp Bot* 60:197-212.
27. Obayashi T, et al. (2009) ATTED-II provides coexpressed gene networks for Arabidopsis. *Nucleic Acids Res* 37:D987-991.
28. Ojangu EL, Jarve K, Paves H, Truve E (2007) Arabidopsis thaliana myosin XIK is involved in root hair as well as trichome morphogenesis on stems and leaves. *Protoplasma* 230:193-202.
29. Hachikubo Y, et al. (2007) Enzymatic activity and motility of recombinant *Arabidopsis* myosin XI, MYA1. *Plant Cell Physiol.* 48:886-891.
30. Reddy AS, Day IS (2001) Analysis of the myosins encoded in the recently completed Arabidopsis thaliana genome sequence. *Genome Biol* 2:RESEARCH0024.
31. Sparkes IA, Ketelaar T, Ruijter NC, Hawes C (2009) Grab a Golgi: Laser trapping of Golgi bodies reveals in vivo interactions with the endoplasmic reticulum. *Traffic* 10:567-571.
32. Hoffmann A, Nebenfuhr A (2004) Dynamic rearrangements of transvacuolar strands in BY-2 cells imply a role of myosin in remodeling the plant actin cytoskeleton. *Protoplasma* 224:201-210.
33. Holweg CL (2007) Living markers for actin block myosin-dependent motility of plant organelles and auxin. *Cell Motil Cytoskeleton* 64:69-81.
34. Boevink P, et al. (1998) Stacks on tracks: the plant Golgi apparatus traffics on an actin/ER network. *Plant J* 15:441-447.
35. Higaki T, et al. (2006) Actin microfilaments regulate vacuolar structures and dynamics: dual observation of actin microfilaments and vacuolar membrane in living tobacco BY-2 Cells. *Plant Cell Physiol* 47:839-852.
36. Nakano TR, et al. (2009) GNOM-LIKE1/ERMO1 and SEC24a/ERMO2 Are Required for Maintenance of Endoplasmic Reticulum Morphology in Arabidopsis thaliana. *Plant Cell* 21:3672-3685.
37. Staiger CJ, et al. (2009) Actin filament dynamics are dominated by rapid

growth and severing activity in the Arabidopsis cortical array. *J Cell Biol* 184:269-280.
38. Matsushima R, et al. (2003) The ER body, a novel endoplasmic reticulum-derived structure in Arabidopsis. *Plant Cell Physiol* 44:661-666.
39. Mano S, et al. (2002) Distribution and characterization of peroxisomes in Arabidopsis by visualization with GFP: dynamic morphology and actin-dependent movement. *Plant Cell Physiol* 43:331-341.
40. Mitsuhashi N, et al. (2000) Characterization of organelles in the vacuolar-sorting pathway by visualization with GFP in tobacco BY-2 cells. *Plant Cell Physiol* 41:993-1001.
41. Nakagawa T, et al. (2007) Improved Gateway binary vectors: high-performance vectors for creation of fusion constructs in transgenic analysis of plants. *Biosci Biotechnol Biochem* 71:2095-2100.
42. Clough SJ, Bent AF (1998) Floral dip: a simplified method for Agrobacterium-mediated transformation of Arabidopsis thaliana. *Plant J* 16:735-743.
43. Shimada T, et al. (2003) Vacuolar processing enzymes are essential for proper processing of seed storage proteins in Arabidopsis thaliana. *J Biol Chem* 278:32292-32299.
44. Hatano K, et al. (1997) A rapid increase in the level of binding protein (BiP) is accompanied by synthesis and degradation of storage proteins in pumpkin cotyledons. *Plant Cell Physiol* 38:344-351.
45. Dhugga KS, Tiwari SC, Ray PM (1997) A reversibly glycosylated polypeptide (RGP1) possibly involved in plant cell wall synthesis: purification, gene cloning, and trans-Golgi localization. *Proc Natl Acad Sci U S A* 94:7679-7684.

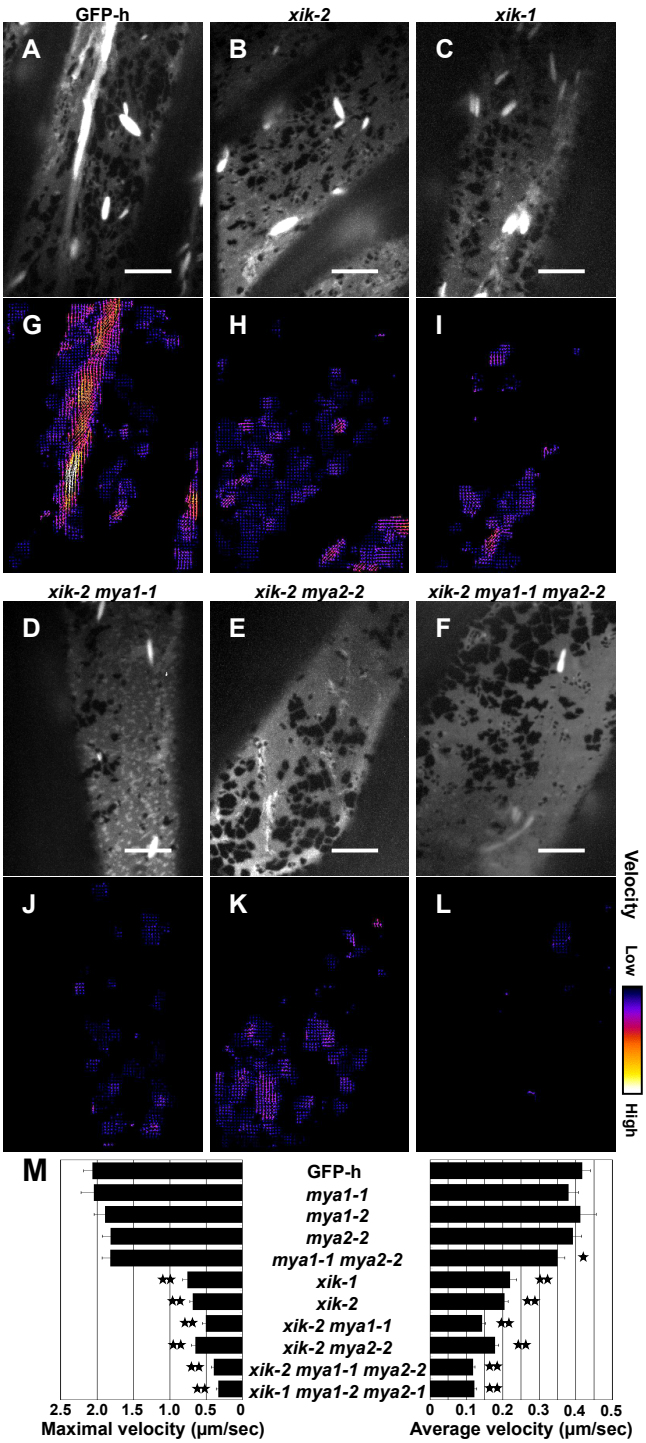

Fig. 1. ER streaming is suppressed in myosin XI-K–deficient mutants. Seven-day-old cotyledonary petioles of GFP-h and myosin XI mutants expressing ER-localized GFP were observed by spinning-disk confocal microscopy. One-hundred time-lapse images of sub-peripheral ER were captured at ~50-ms intervals. Single mutants lacking myosin XI-K [*xik-1*, SALK_136682; *xik-2*, SALK_067972], MYA1/XI-1 [*mya1-1*, SALK_129098; *mya1-2*, SALK_022140], or MYA2/XI-2 [*mya2-1*, SALK_127984; *mya2-2*, SALK_055785] and double and triple mutants were generated. Maximum intensity projections (*A-F*) and velocity maps (*G-L*) of the GFP-h or mutant time-lapse images are shown. Bright spindle-shaped structures are ER bodies. Scale bars, 10 μm. Arrow lengths and colors in the maps indicate ER streaming velocities. (*M*) Maximal and average velocities (μm/sec) of ER streaming in GFP-h and mutants were calculated by KbiFlow software. Error bars represent S. E.. *, $P < 0.05$; **, $P < 0.001$ by Student's *t*-test.

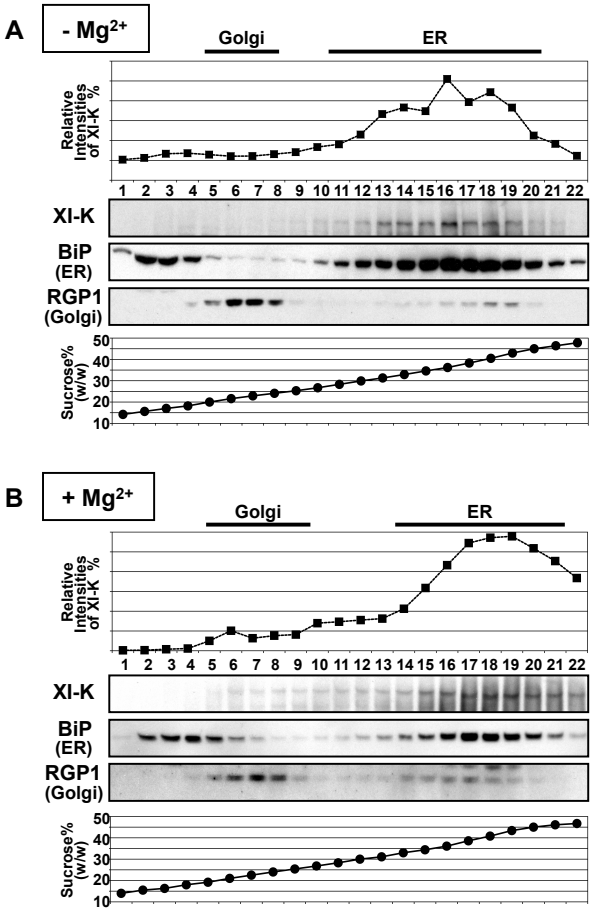

Fig. 2. Co-fractionation of myosin XI-K with ER. Microsomal fractions prepared from 17-day-old plants in the presence of either EDTA (-Mg^{2+}; *A*) or $MgCl_2$ (+Mg^{2+}; *B*) were subjected to sucrose density gradient (15% to 50%, w/w) centrifugation in the presence of EDTA (-Mg^{2+}; *A*) or $MgCl_2$ (+Mg^{2+}; *B*). Fractions were subjected to immunoblot analysis with antibodies against myosin XI-K, BiP (ER marker), or RGP1 (Golgi marker).

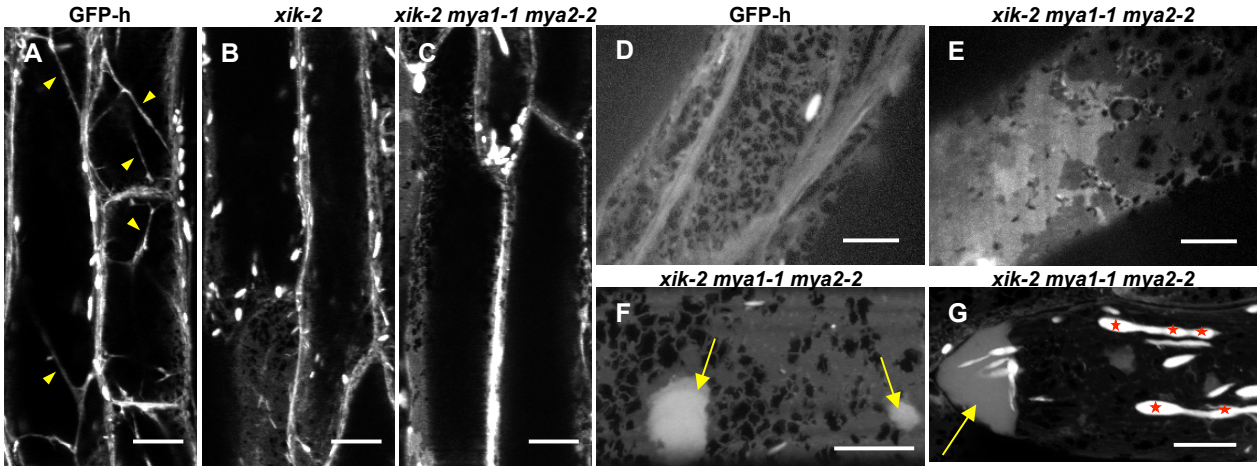

Fig. 3. Myosin XI-K deficiency induces an aberrant ER configuration. Maximum intensity projections of 8-day-old (*A-C*) or 7-day-old (D-G) GFP-h (*A, D*), *xik-2* (*B*), and *xik-2 mya1-1 mya2-2* (*C, E-G*) cotyledonary petioles expressing ER-localized GFP observed by laser-scanning confocal microscopy (*A-C*, *F*, *G*) or spinning-disk confocal microscopy (*D*, *E*). Projections were reconstituted from six (*A-C*) or four (*F-G*) sequential images taken along the optical z-axis (1 μm intervals), or from 100 time-sequential images of sub-peripheral ER captured at ~50-ms intervals (*D, E*). Bright spindle-shaped structures are ER bodies; Arrowheads in *A* indicate transvacuolar strands; Yellow arrows in *F* and *G* indicate ER aggregates; Red asterisks in *G* indicate abnormally shaped ER bodies. Scale bars, 20 μm (*A-C*) or 10 μm. (*D-G*).

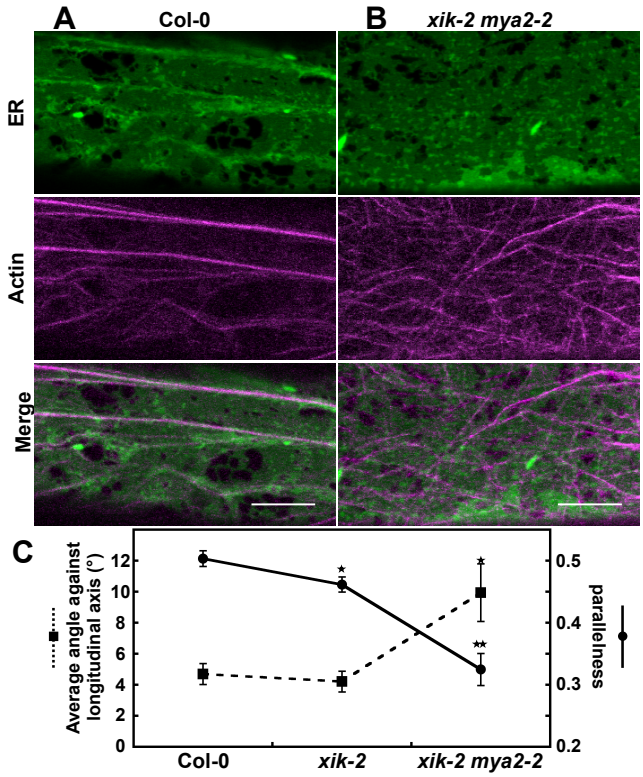

Fig. 4. Myosin XI-K deficiency induces AF-bundle disorganization. Seven-day-old cotyledonary petioles of Col-0 (*A*) and *xik-2 mya2-2* (*B*) expressing ER-localized GFP and tdTomato-ABD2 were observed by laser-scanning confocal microscopy. Maximum intensity projections were reconstituted from three sequential images taken along the optical *z*-axis (0.5 μm intervals). Scale bars, 10 μm. Orientation of AF-bundles was evaluated by two indices: Average angle of AF-bundles against a longitudinal axis and parallelness. Error bars represent S. E.. *, $P < 0.05$; **, $P < 0.001$ by Student's *t*-test (n=24-26).

Supplemental Information

Materials and Methods

Development of a New Software, KbiFlow, for Quantitative Analysis of ER streaming. To measure the velocity of ER streaming, an optical flow analysis was performed based on cross-correlation function (1, 2). As a preprocessing stage, immobile components were filtered by the subtraction of temporal-averaged image (3).

$$\mathrm{I}(x,y,t) = \mathrm{I}_{\mathrm{raw}}(x,y,t) - \sum_{t'=0}^{T-1} \frac{\mathrm{I}_{\mathrm{raw}}(x,y,t')}{T} \quad , \qquad [1]$$

where I_{raw} is the original stack, I is the preprocessed stack, T is the total number of frames (100), x and y are spatial variables, and t is a temporal variable (frame index). Next, we measured the velocity vector for each pixel using spatial-temporal correlation analysis. To reduce the error vectors, a 3 x 3 median filter was applied as a postprocessing stage. As a result, a velocity map, F, was obtained for each stack.

$$\Delta \mathrm{I}(x,y,t) = \mathrm{I}(x,y,t) - \frac{\sum_{u,v \in N} \mathrm{I}(x+u, y+v, t)}{\|N\|} \quad , \qquad [2]$$

$$\mathrm{Corr}_{\,\mathrm{average}}(x,y,\tau,\xi,\eta) = \sum_{t=0}^{T-1-\tau} \frac{\sum_{u,v \in N} \Delta \mathrm{I}(x+u,y+v,t) \cdot \Delta \mathrm{I}(x+u+\xi, y+v+\eta, t+\tau)}{(T-\tau)\sqrt{\sum_{u,v \in N} \Delta \mathrm{I}(x+u,y+v,t)^2 \cdot \sum_{u,v \in N} \Delta \mathrm{I}(x+u+\xi, y+v+\eta, t+\tau)^2}} \quad ,$$

[3]

$$\vec{\mathrm{F}}(x,y) = \underset{u,v \in (-1,0,+1)}{\mathrm{median}} \left[\sum_{\tau=1}^{T-1} \frac{\underset{\vec{f}=(\xi,\eta) \in N}{\mathrm{argmax}} \left\{ \mathrm{Corr}_{\,\mathrm{average}}(x+u, y+v, \tau, \xi, \eta) \right\}}{\tau (T-1)} \right] \quad , \qquad [4]$$

where ΔI is relative intensity, $Corr_{average}$ is the temporal ensemble of the spatio-temporal correlation function, ξ and η are spatial lag variables, τ is the

temporal lag variable, f is the velocity vector, F is the map of velocity vectors. N consists of 16 x 16 neighbor pixels (-8 < u,v ≤ +8) and $\|N\|$ is 256.

The velocity map F contained ER regions and non-ER regions, such as vacuoles and extra-cellular regions. Since the non-ER regions were not necessary for velocity analysis of ER, we generated a mask image M to remove the non-ER regions.

$$\mathrm{M}(x,y) = \begin{cases} 1 & if \quad 1 - 2\mathrm{Corr}_{\,\mathrm{average}}(x,y,1,0,0) + \mathrm{Corr}_{\,\mathrm{average}}(x,y,2,0,0) < n \\ 0 & otherwise \end{cases}, \qquad [5]$$

where n is the threshold of the noise component (n = 0.8 for the statistical analysis of ER streaming in Fig. 1*M* and Table S1 and n = 0.95 for the generation of the velocity distribution maps). To calculate an average velocity and a maximal velocity, we applied the mask image M to the velocity map F using the following equations.

$$Velocity_{\,average} = \frac{\sum_{x,y \in all} \mathrm{M}(x,y) \left| \vec{\mathrm{F}}(x,y) \right|}{\sum_{x,y \in all} \mathrm{M}(x,y)}, \qquad [6]$$

$$Velocity_{\,max} = \max_{x,y \in all} \left\{ \mathrm{M}(x,y) \left| \vec{\mathrm{F}}(x,y) \right| \right\}. \qquad [7]$$

ER streaming was analyzed using our in-house developed plugin package for ImageJ software. Calculation and statistical analysis of velocities were performed by KbiFlow plugin (eq1-4, 6,7). Mask images were generated from 'estimateNoise' mode of KbiStkFilter plugin (eq 5). The KBI plugin package can be downloaded for free from http://hasezawa.ib.k.u-tokyo.ac.jp/zp/Kbi/ImageJKbiPlugins. Scheme of velocity analysis for ER streaming is shown in Fig. S1.

Quantitative Analysis of Cytosol streaming. Cytosol streaming was analyzed by the KbiFlow plugin essentially as the analysis of ER streaming. Due to low signal-to-noise ratio in this analysis, we increased the threshold of the noise component up to 0.9 and selected the cells having more than 100 successful measurement points.

Image Analysis of Actin Filament Bundles. To evaluate AF-bundles orientations quantitatively, we measured average angles and parallelness of AF-bundles by

image processing. We firstly extracted AF-bundles as skeletonized images from confocal images by multi-directional non-maximum suppression (MDNMS) algorithm (Fig. S8*A*) (4). As preprocess and postprocess of MDNMS, noise in the image was reduced by gradient inverse weighted smoothing filter (5) and morphological filters. In the skeletonized images, angles of a neighbored pixel pair could be categorized into 0, 45, 90 and 135 against the longitudinal axis of cell, and their pixel numbers were counted, basically according to our previous study (6). The average angle is defined by

$$\theta = \begin{cases} \arctan \dfrac{|n_{45} - n_{135}|}{|n_0 - n_{90}| + |n_{45} - n_{135}|} & if\ n_0 \geq n_{90}\ and\ n_{45} > n_{135} \\ 90^\circ + \arctan \dfrac{|n_{45} - n_{135}|}{|n_0 - n_{90}| + |n_{45} - n_{135}|} & if\ n_0 < n_{90}\ and\ n_{45} \geq n_{135} \\ 90^\circ - \arctan \dfrac{|n_{45} - n_{135}|}{|n_0 - n_{90}| + |n_{45} - n_{135}|} & if\ n_0 < n_{90}\ and\ n_{45} < n_{135} \\ 180^\circ - \arctan \dfrac{|n_{45} - n_{135}|}{|n_0 - n_{90}| + |n_{45} - n_{135}|} & if\ n_0 \geq n_{90}\ and\ n_{45} < n_{135}, \end{cases} \quad [8]$$

where n0, n45, n90 and n135 are the numbers of the pixel pair, which form the 0, 45, 90 and 135, respectively. The parallelness is defined by

$$P = \frac{|n_0 - n_{90}| + |n_{45} - n_{135}|}{n_0 + n_{45} + n_{90} + n_{135}} \quad [9]$$

and can range from 0 to 1. The parallelness becomes higher as the AF-bundles run parallel each other. All procedures were automatically performed using our ImageJ plug-ins: KbiLineExtract and KbiLineFeature which can be invoked by Kbi_Filter2d plug-ins (filter = lineFilters, lineMode = lineExtract or lineFeature). In this study, all parameters of KbiLineExtract were fixed as follows: giwsIter = 5, mdnmsLen = 20, pickup = ostu, shaveLen = 5, delLen = 10.

RT-PCR and Genotyping. Total RNA was isolated from the 7-day-old *Arabidopsis* seedling with an RNeasy plant mini kit (Qiagen, Valencia, CA). Total RNA (1 μg) was subjected to first-strand cDNA synthesis using Ready-To-Go RT-PCR Beads (GE Healthcare, Buckinghamshire, UK). An aliquot (1 μl) was subjected to PCR with Ex Taq polymerase (Takara, Otsu, Japan). The following gene-specific primers are used for RT-PCR and genotyping: MYA1-F, 5'-CTGCAATTGTTTTGCAATCCTTCCTACGAG-3'; MYA1-R, 5'-CTCGAGCCGCCTCCTGTTCCTTTACGACCA-3'; MYA2-F, 5'-AAAGATTACGTTATTGCCGAGCATCAGGCA-3'; MYA2-R2,

5’-GTGATCTTATCCATTAATTCCTGATCAACC-3’; MYA2-F3, 5’-TCGATTCTACCCTGATGAAG-3’; MYA2-R4, 5’-TCACCAAGAATGAGCAATCG-3’; XIK-F, 5’-ATCGCAAACGTATTTCCAAAGGATACAGAG-3’; XIK-R, 5’-CTCCCACAGTTGTCAAACTGAAGCTCGACA-3’; XIK-F2, 5’-GTTTCCAGAATGAAGGAAACTGAGGG-3’; XIK-R2, 5’-ACTCATATGTTAGAGGAGTAACACGG-3’; XIK-F3, 5’-CACAGGACATGACTCTTGCTGTACG-3’; XIK-R3, 5’-GCACTTTGAGGAGATCCCCTTAATCC-3’; Actin-F, 5’-AGAGATTCAGATGCCCAGAAGTCTTGTTCC-3’; Actin-R, 5’-GAGTATGATGAGGCAGGTCCAGGAATCGTT-3’; and T-DNA left border (LBa1), 5’-TGGTTCACGTAGTGGGCCATCG-3’.

Treatments with Latrunculin B and 2,3-Butanedione Monoxime. Stock solutions of reagents used were 5 mM latrunculin B (Lat B) in DMSO and 1 M 2,3-butanedione monoxime (BDM) in H_2O. Seven-day-old seedlings of GFP-h were incubated in water containing Lat B (0, 2.5, 5.0, 10, 20 μM) and BDM (0, 25, 50, 75 mM) under vacuum.

Etiolated Hypocotyls. Seeds of *Arabidopsis* were surface-sterilized and then sown onto 0.5% Gellan Gum (Wako, Tokyo, Japan) that contained 1% sucrose and Murasige-Skoog's medium. After incubation for 3 days at 4˚C to break seed dormancy, the plants were grown at 22˚C in the light for 2 h and then in the dark for 72 h.

Phalloidin Staining. Phalloidin staining of AF-bundles with Alexa Fluor 546 phalloidin was performed as described previously (7).

References

1. Hebert B, Costantino S, Wiseman PW (2005) Spatiotemporal image correlation spectroscopy (STICS) theory, verification, and application to protein velocity mapping in living CHO cells. *Biophys J* 88**:**3601-3614.
2. Ji L, Danuser G (2005) Tracking quasi-stationary flow of weak fluorescent signals by adaptive multi-frame correlation. *J Microsc* 220**:**150-167.
3. Brown CM, et al. (2006) Probing the integrin-actin linkage using high-resolution protein velocity mapping. *J Cell Sci* 119**:**5204-5214.
4. Sun C, Vallotton P (2009) Fast linear feature detection using multiple directional non-maximum suppression. *J Microsc* 234**:**147-157.
5. Wang DCC, Vagnucci AH, Li CC (1981) Gradient inverse weighted smoothing scheme and the evaluation of its performance. *Comp Graph Image Proc* 15**:**167-181.

6. Yoneda A, et al. (2007) Chemical genetic screening identifies a novel inhibitor of parallel alignment of cortical microtubules and cellulose microfibrils. *Plant Cell Physiol* 48**:**1393-1403.
7. Tamura K, et al. (2005) KATAMARI1/MURUS3 Is a novel golgi membrane protein that is required for endomembrane organization in Arabidopsis. *Plant Cell* 17**:**1764-1776.

Legends for Supplementary Movies

Movie S1. ER Streaming in GFP-h.
This is a real-time movie corresponding to Fig. S2*A*.

Movie S2. ER Streaming in GFP-h.
This is a real-time movie corresponding to Fig. S2*B*.

Movie S3. Streaming of Cytosolic GFP.
This is a real-time movie corresponding to Fig. S3*B*.

Movie S4. ER Streaming Is Suppressed with an Actin-Depolymerizing Reagent.
This is a real-time movie corresponding to Fig. S4*C*.

Movie S5. ER Streaming Is Suppressed with a Myosin Inhibitor.
This is a real-time movie corresponding to Fig. S4*F*.

Movie S6. ER Streaming Is Suppressed in *xik*.
This is a real-time movie corresponding to Fig. 1*B*.

Movie S7 ER Streaming Is Suppressed in *xik mya1 mya2*.
This is a real-time movie corresponding to Fig. 1*F*.

Movie S8. ER Aggregates in *xik mya1 mya2*.

ER aggregates corresponding to Fig. 3*G* are shown as three-dimensional structures that were reconstituted from 14-sequential confocal images taken along the optical z-axis (1 μm intervals).

Movie S9. ER Streaming in the Elongating Cell of Etiolated GFP-h Hypocotyl.
This is a real-time movie.

Movie S10 ER Streaming Is Suppressed in the Elongating Cell of Etiolated *xik mya2* Hypocotyl.
This is a real-time movie.

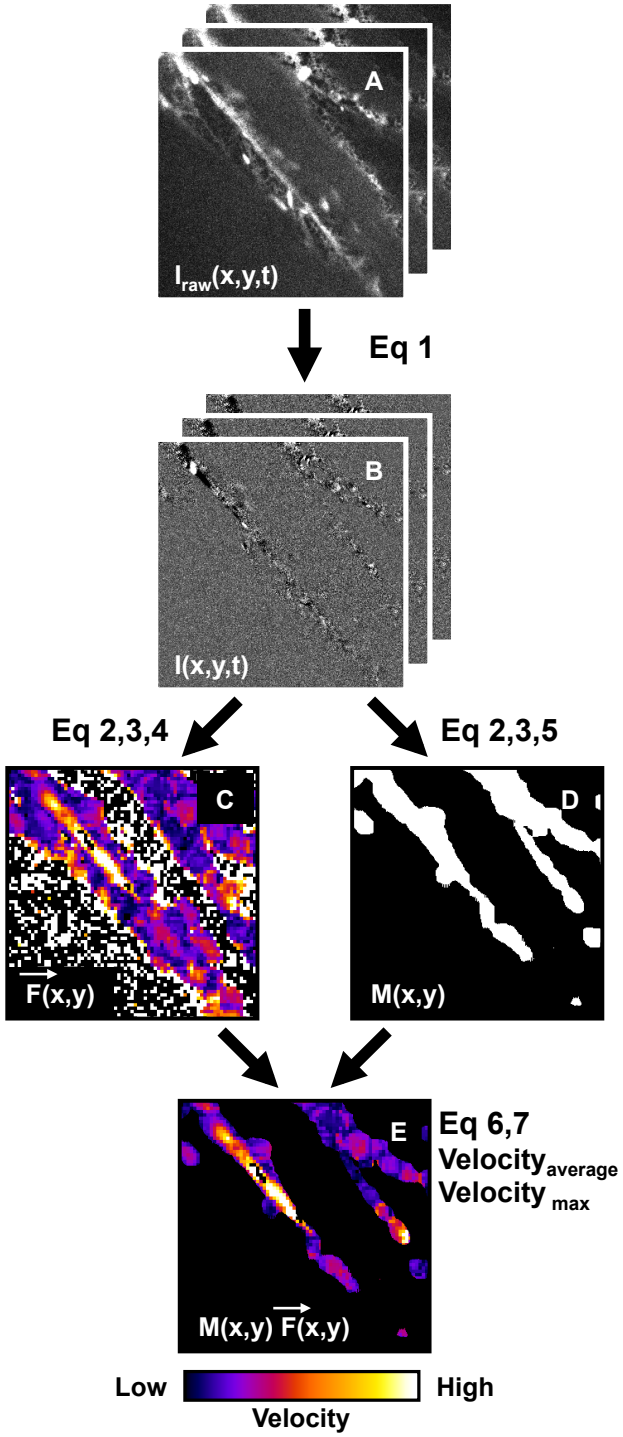

Fig. S1. Velocity analysis scheme for ER streaming. (*A*) Original stack of time-lapse images. (*B*) Preprocessed stack. (*C*) Velocity distribution map. Color represents the velocity. Note that there are some error vectors outside of the ER regions (white pixels). (*D*) Mask image indicates ER region. White: 1, black: 0. (*E*) Masked velocity distribution map. Average and maximal velocities were calculated from *E* based on Eqns. 6 and 7.

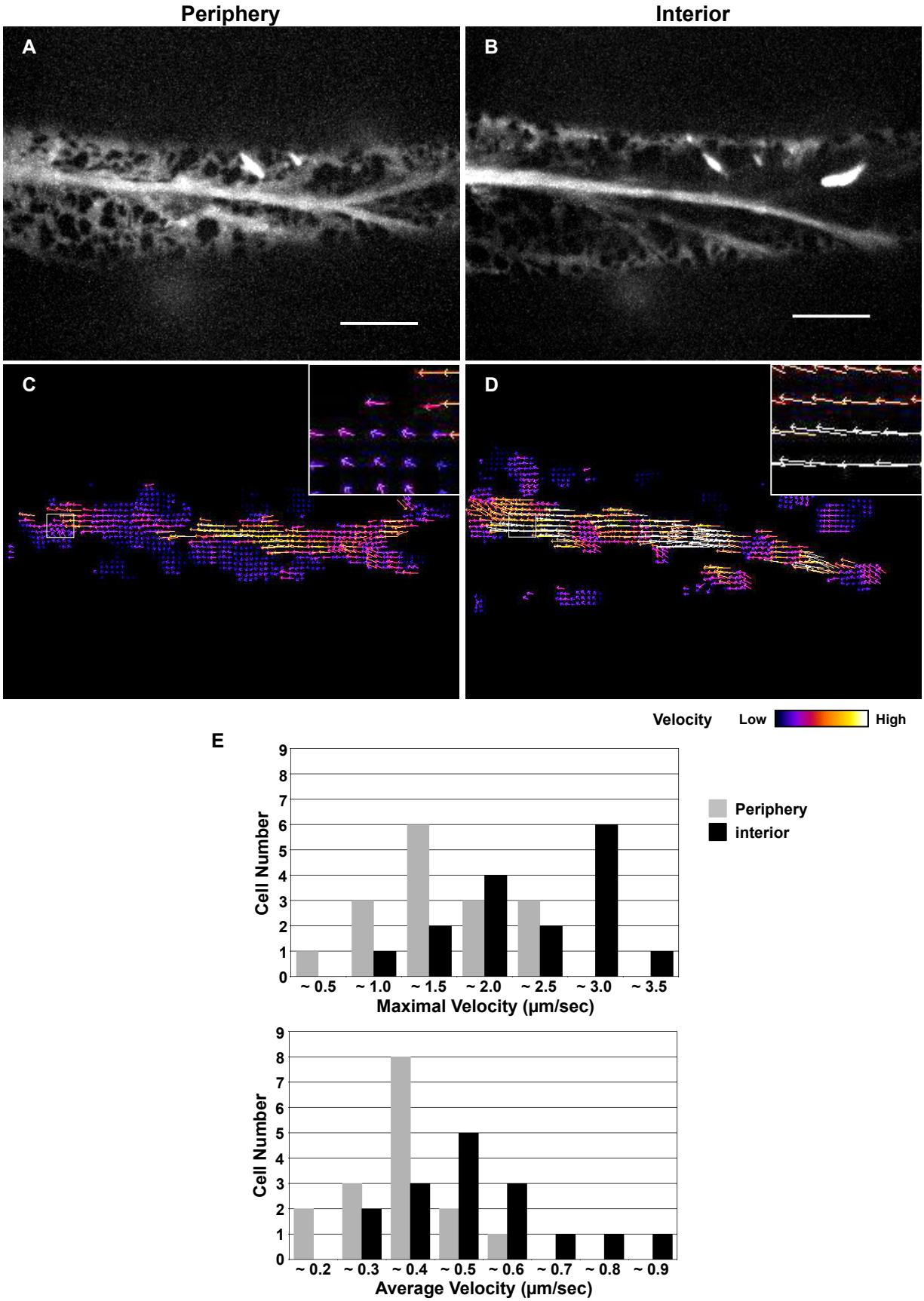

Fig. S2. Endoplasmic reticulum (ER) streaming velocity map using our developed KbiFlow software. Seven-day-old GFP-h cotyledonary petioles were observed by spinning-disk confocal microscopy. We captured 100 images of GFP-labeled ER at ~50-ms intervals in two ~1-μm-thick optical planes at ~1.5 μm distance, a peripheral plane and an interior plane, of a cell. (*A* and *B*) Maximum intensity projection of the time-lapse images of each plane. Bright trails indicate ER streaming. Scale bars, 10 μm. (*C* and *D*) Velocity map generated by processing the time-lapse images (*A* and *B*) with KbiFlow. Arrow lengths and colors indicate ER streaming velocities. Insets are magnified views of the boxed areas in the maps. (*E*) Histograms of the maximal velocity and the average velocity.

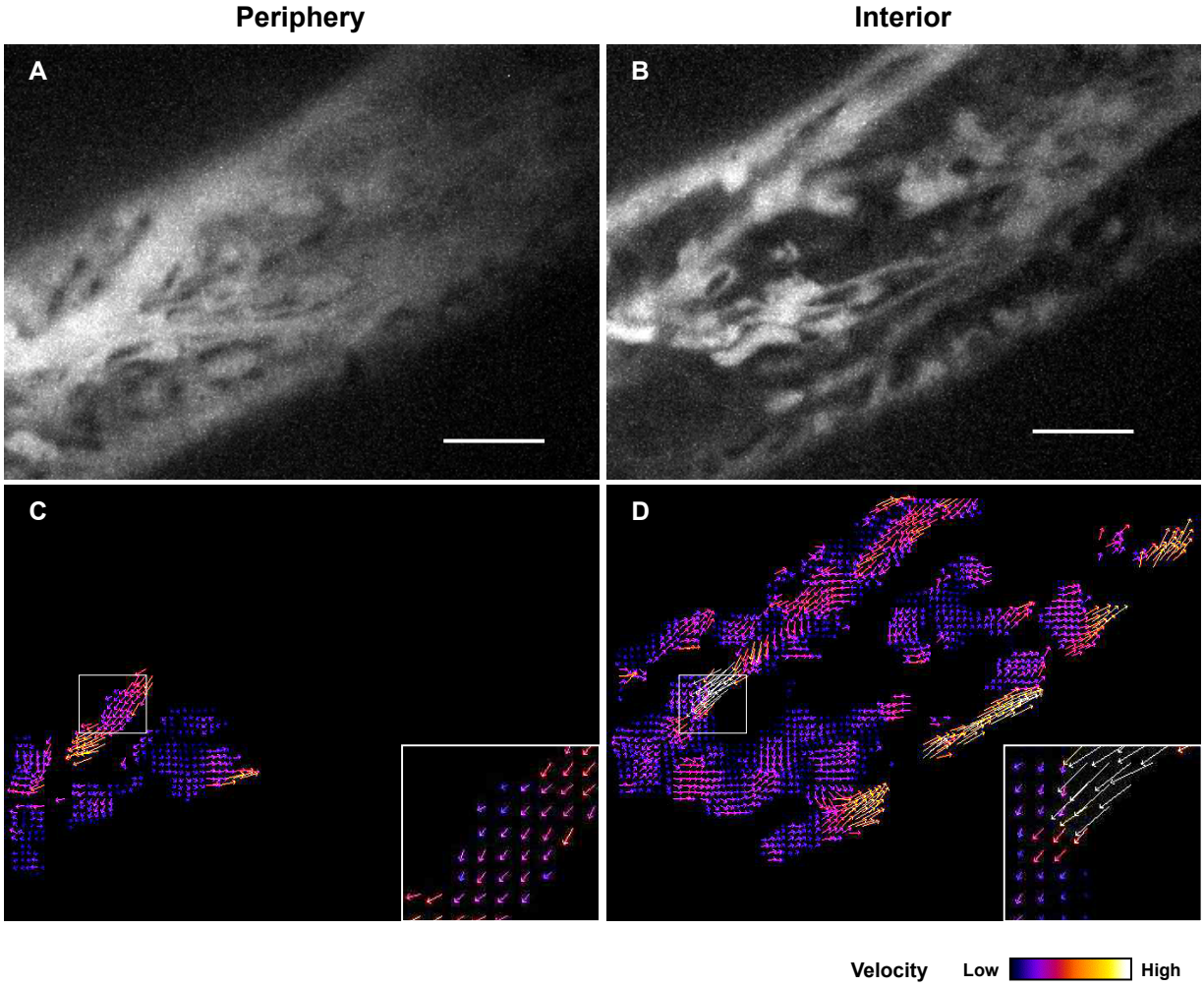

Fig. S3. Cytosol streaming velocity map using KbiFlow software. Seven-day-old cotyledonary petioles of cytosolic GFP-expressing transgenic plant were observed by spinning-disk confocal microscopy. We captured 100 images of GFP-labeled cytosol at ~50-ms intervals in two ~1-μm-thick optical planes at ~1.5 μm distance, a peripheral plane and an interior plane, of a cell. (*A* and *B*) Maximum intensity projection of the time-lapse images of each plane. Bright trails indicate cytosol streaming. Scale bars, 10 μm. (*C* and *D*) Velocity map generated by processing the time-lapse images (*A* and *B*) with KbiFlow. Arrow lengths and colors indicate streaming velocities. Insets are magnified views of the boxed areas in the maps.

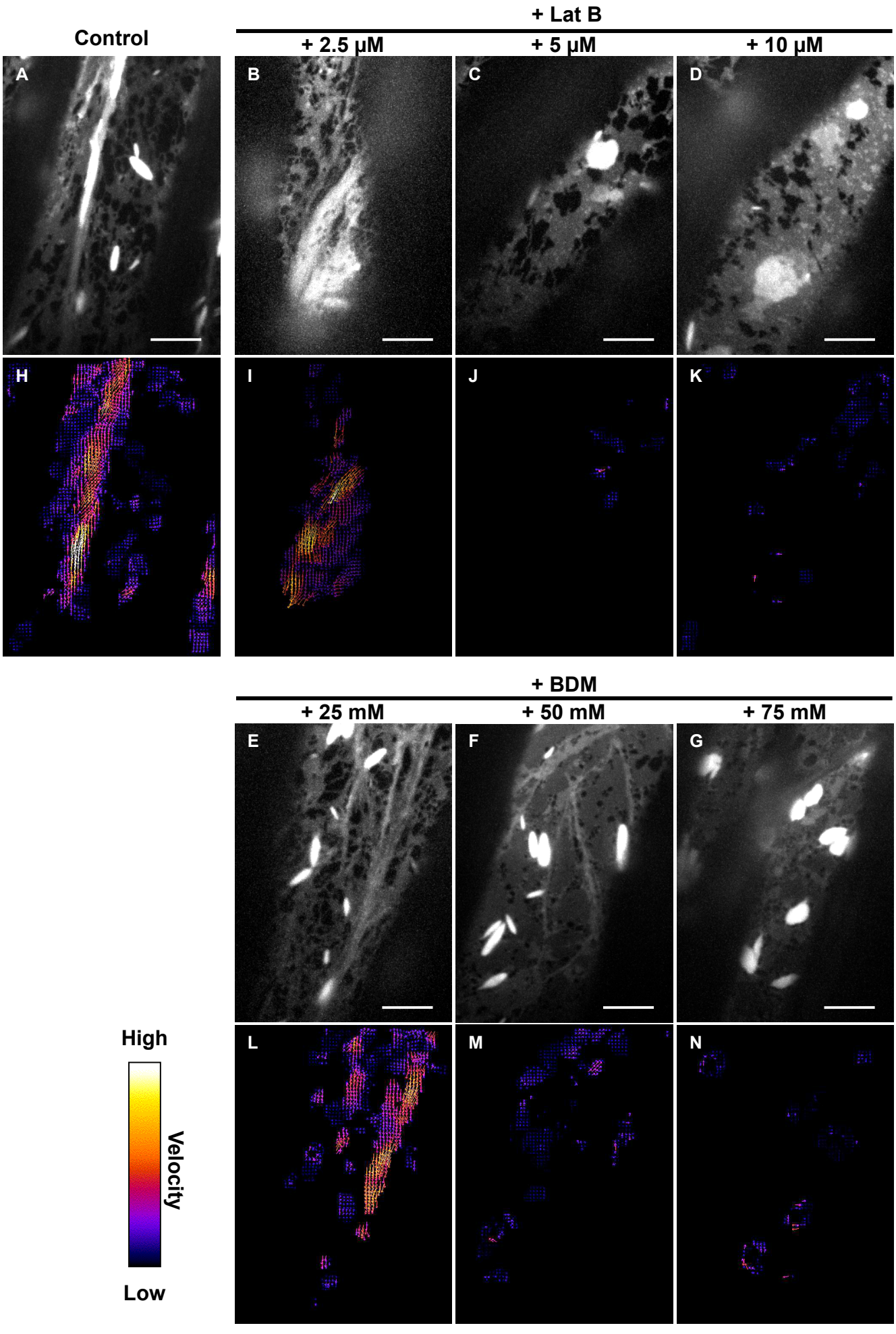
Control
+ Lat B
+ 2.5 µM
+ 5 µM
+ 10 µM
A
B
C
D
H
I
J
K
+ BDM
+ 25 mM
+ 50 mM
+ 75 mM
E
F
G
L
M
N
High
Velocity
Low

Fig. S4. ER streaming is suppressed by an actin-depolymerizing reagent or myosin inhibitor. Seven-day-old cotyledonary petioles of GFP-h were observed by spinning-disk confocal microscopy. We captured 100 images of GFP-labeled ER at ~50-ms intervals. (*A*-*G*) Maximum intensity projections of the time-lapse ER streaming images. Bright spindle-shaped structures are ER bodies. Scale bars, 10 μm. (*H*-*N*) Velocity maps corresponding to *A*-*G*, respectively. Velocities are represented by arrow lengths and arrow colors. (*A* and *H*) Control image. (*B*-*D* and *I*-*K*) Time-lapse images of sub-peripheral ER acquired after treatment with latrunculin B (Lat B; an actin-depolymerizing reagent) for 20 min~1.5 h. ER aggregates were forming, but they were slowly streaming after the treatment of 2.5 μM Lat B for 1.5 h. On the other hand, ER streaming was completely inhibited by the treatments with 5 or 10 μM Lat B for 40 or 20 min, respectively. (*E*-*G* and *L*-*N*) Time-lapse images of sub-peripheral ER acquired after treatment with 2,3-butanedione monoxime (BDM; a myosin inhibitor) for 30 min~1 h. ER streaming was observed after the treatment of 25 mM BDM for 1 h, whereas ER streaming was completely inhibited after the treatments with 50 or 75 mM BDM for 40 min. The spindle-shaped ER bodies were collapsed by the treatment of 75 mM BDM.

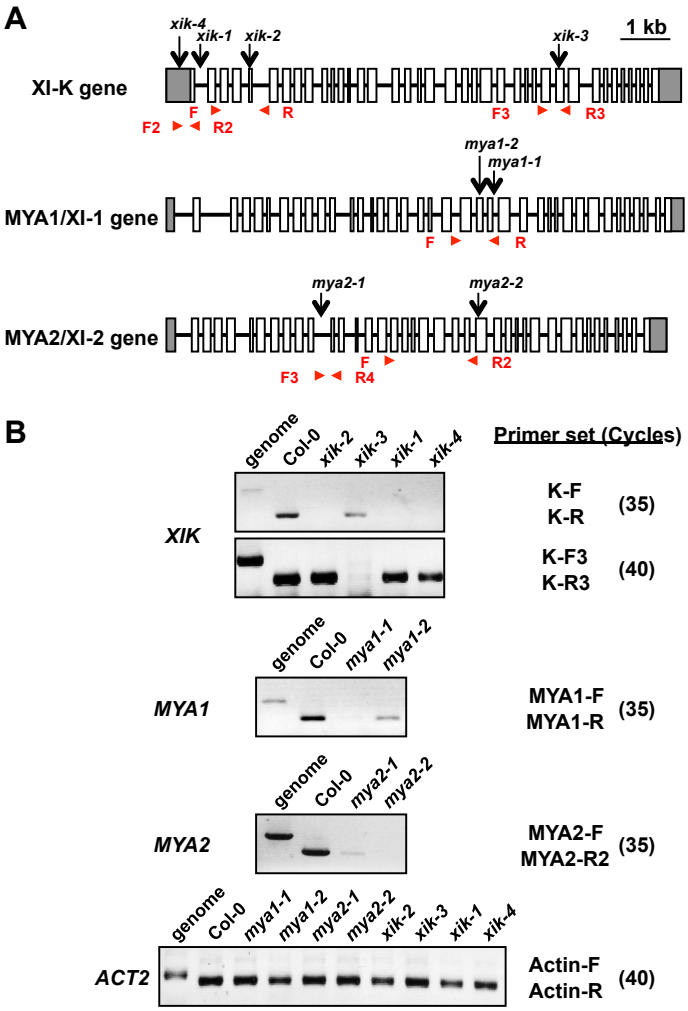

Fig. S5. Isolated myosin XI mutants. (*A*) Structures of the MYA1/XI-1, MYA2/XI-2, and XI-K genes. White boxes, gray boxes, and black lines show exons, untranslated regions, and introns, respectively. The position of each T-DNA insertion is indicated for XI-K gene (xi*k-1*, SALK_136682; xi*k-2*, SALK_067972; xi*k-3*, SALK_018764; *xik-4*, SALK_152496), MYA1/XI-1 gene (*mya1-1*, SALK_129098; *mya1-2*, SALK_022140), and MYA2/XI-2 gene (*mya2-1*, SALK_127984; *mya2-2*, SALK_055785). Primer positions for genotyping and RT-PCR are indicated by red arrowheads. (*B*) RT-PCR analysis of 7-day-old myosin mutant seedlings. The primer sets and number of amplifying cycles used are indicated to the right side of each panel. *ACT2* was used as a loading control.

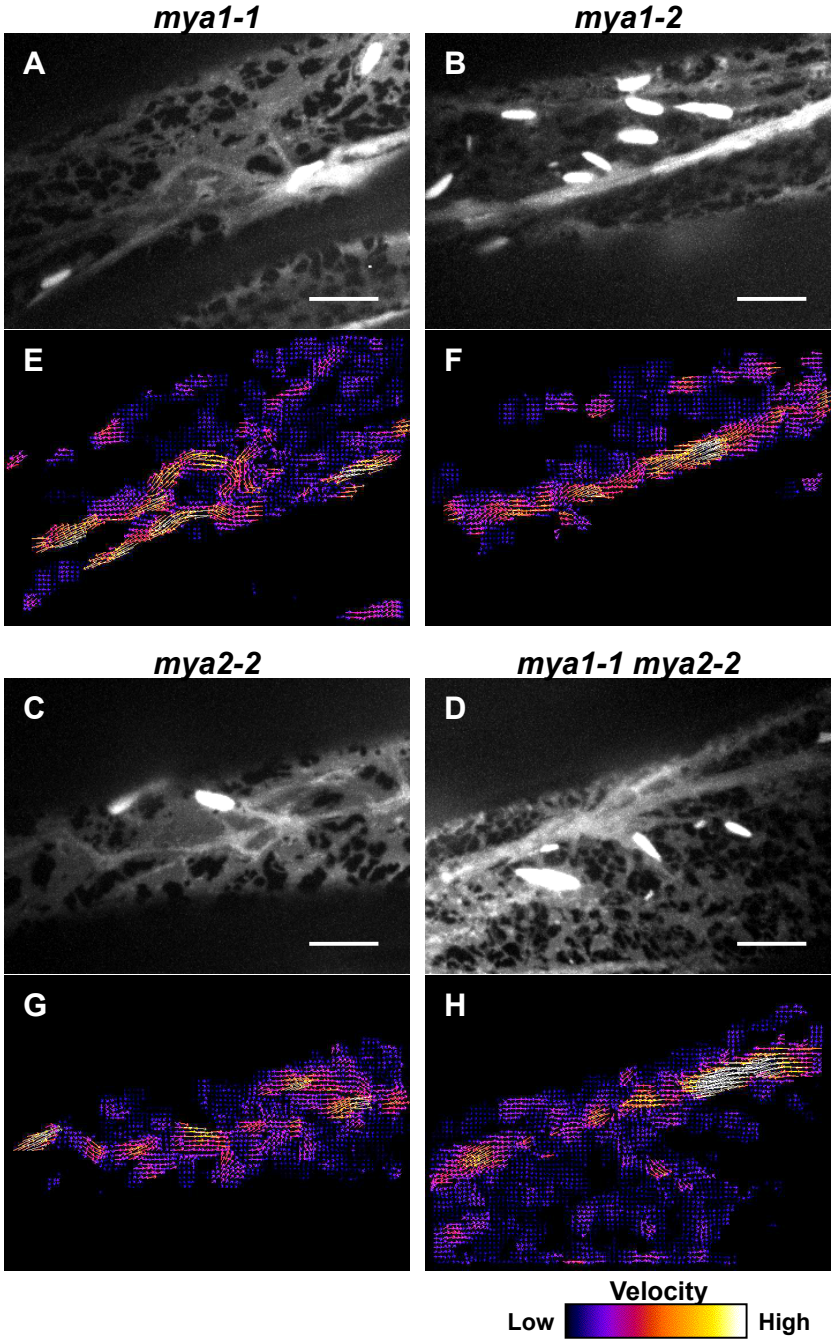

Fig. S6. ER streaming is not suppressed in MYA1/XI-1 or MYA2/XI-2 deficient mutants. Seven-day-old cotyledonary petioles of MYA1/XI-1 or MYA2/XI-2 deficient mutants expressing ER-localized GFP were observed by spinning-disk confocal microscopy. (*A-D*) Maximum intensity projections of 100 time-lapse images of the sub-peripheral ER captured at ~50-ms intervals. Bright spindle-shaped structures are ER bodies. Scale bars, 10 μm. (*E-H*) Velocity maps corresponding to *A-D*, respectively. ER streaming velocities are represented by arrow lengths and arrow colors.

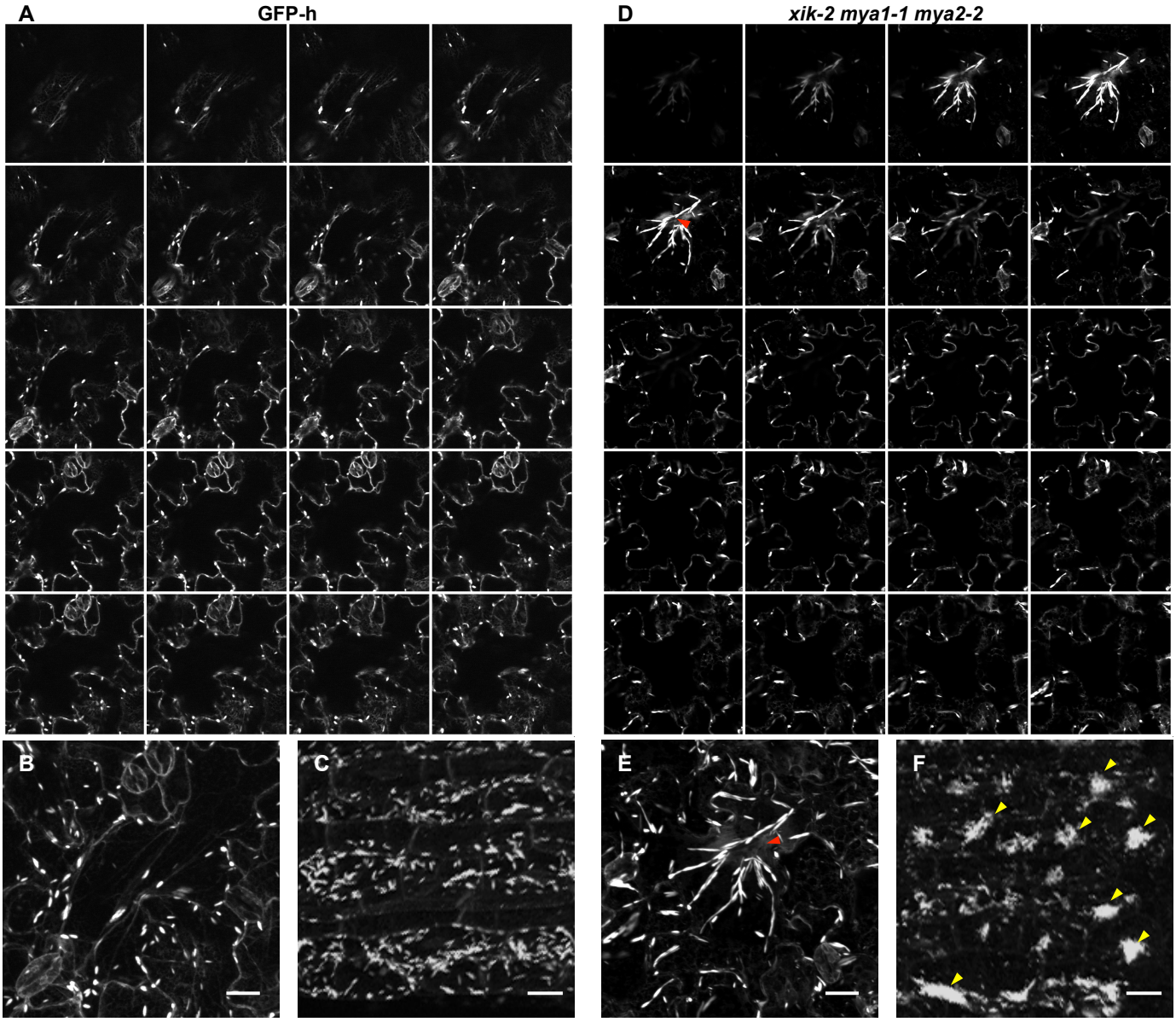

Fig. S7. Myosin XI-K deficiency induces aberrant ER body distributions. Seven-day-old seedlings of GFP-h (*A*-*C*) and *xik-2 mya1-1 mya2-2* (*D*-*F*) expressing ER-localized GFP were observed by laser-scanning confocal microscopy. (*A*, *B*, *D*, and *E*) Epidermal cotyledon cells of GFP-h (*A* and *B*) and *xik-2 mya1-1 mya2-2* (*D* and *E*). ER body distribution patterns are shown as sequential confocal images taken along the optical z-axis (1 μm intervals) (*A* and *D*) and their maximum intensity projections (*B* and *E*). Red arrowhead (*D* and *E*) indicates the nuclear position in a central cell. (*C* and *F*) Hypocotyls of GFP-h (*C*) and *xik-2 mya1-1 mya2-2* (*F*). ER body distribution patterns are shown as maximum intensity projections reconstituted from 22-sequential confocal images taken along the optical z-axis (2 μm intervals). Yellow arrowheads (*F*) indicate aggregates of ER bodies. Scale bars, 20 μm.

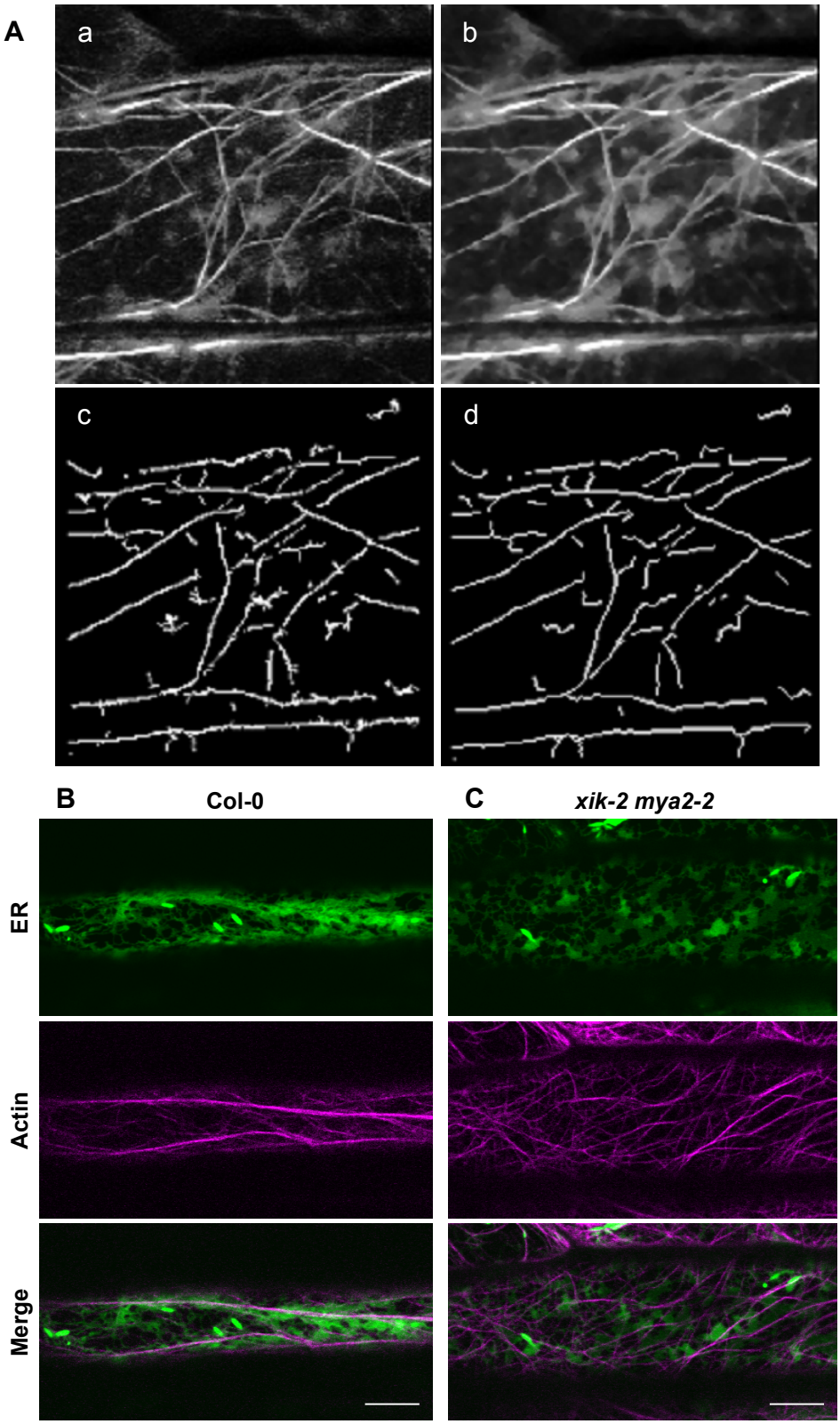

D

	Col-0	*xik-2 mya2-2*
Average angle against longitudinal axis (°)	2.49 (1.65)	6.92 (5.54)*
Parallelness	0.57 (0.07)	0.39 (0.12)**

Fig. S8. Quantitative analysis of the AF-bundle organization. (*A*) Extraction of AF bundles as skeletonized image. (*a*) An original confocal image of actin filaments visualized by tdTomato-ABD2. (*b*) Noise reduced image by gradient inverse weighted smoothing filter. (*c*) Binary image obtained from multi-directional non-maximum suppression algorithm. (*d*) Skeletonization and noise-reduction for the binary image were performed. Average angles and parallelness were measured from the skeletonized image. (*B*-*D*) Myosin XI-K deficiency induces AF-bundle disorganization in the etiolated hypocotyls. Four-day-old etiolated hypocotyls of Col-0 (*B*) and *xik-2 mya2-2* (*C*) expressing ER-localized GFP and tdTomato-ABD2 were observed by laser-scanning confocal microscopy. Scale bars, 10 μm Orientation of AF-bundles was evaluated by two indices: Average angle of AF-bundles against a longitudinal axis and parallelness (*D*). The value in parenthesis represents S. D. *, $P < 0.005$; **, $P < 0.001$ by Student's *t*-test (n=20-24).

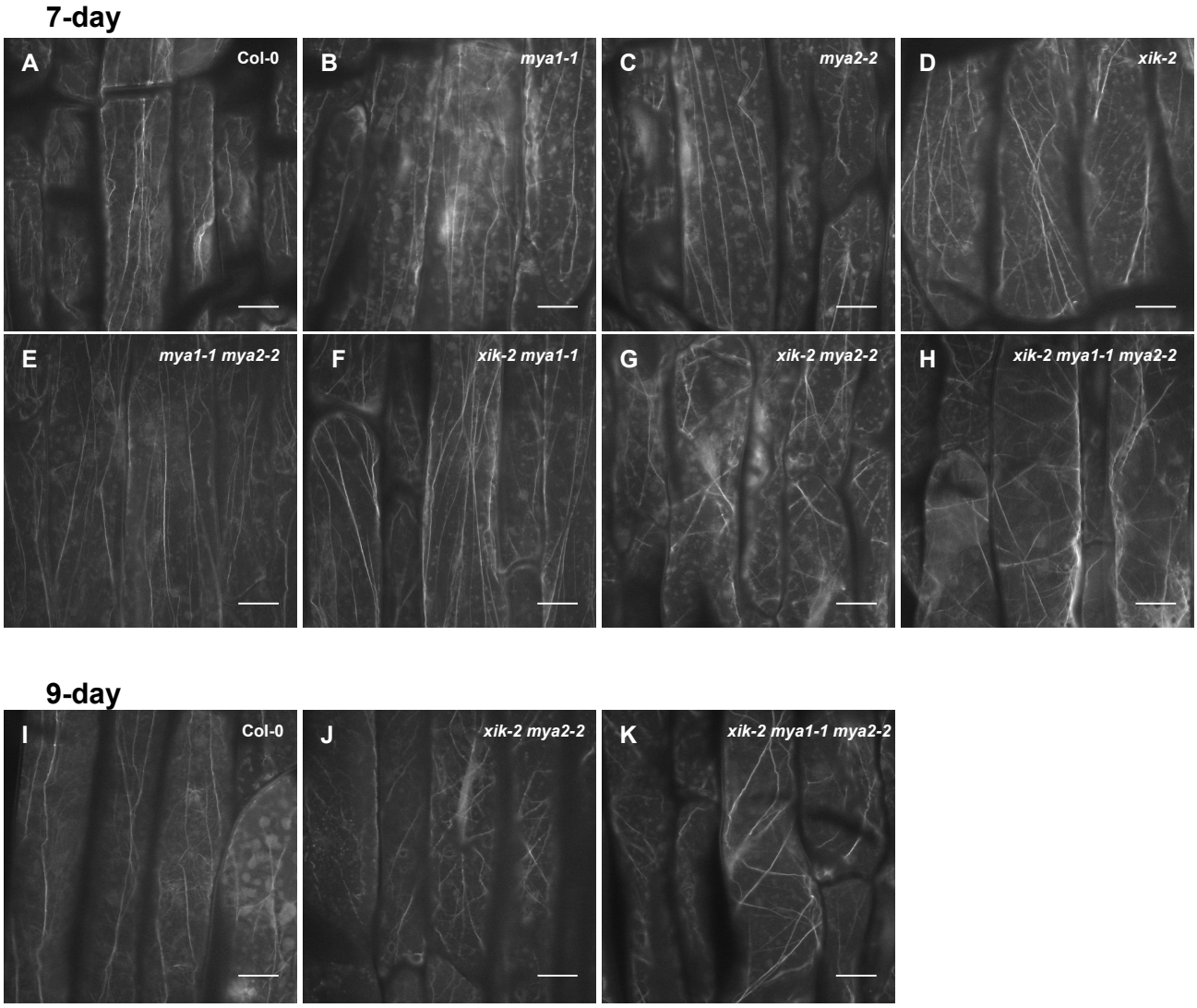

Fig. S9. Myosin XI-K deficiency induces actin filament bundle disorganization. Actin filaments in 7-day-old Col-0 (*A*), *mya1-1* (*B*), *mya2-2* (*C*), *xik-2* (*D*), *mya1-1 mya2-2* (*E*), *xik-2 mya1-1* (*F*), *xik-2 mya2-2* (*G*), and *xik-2 mya1-1 mya2-2* (*H*), and 9-day-old Col-0 (*I*), *xik-2 mya2-2* (*J*), and *xik-2 mya1-1 mya2-2* (*K*) cotyledonary petioles were stained with Alexa Fluor 546 phalloidin. Samples were observed by laser-scanning confocal microscope. Scale bars, 20 μm.

Table S1: Streaming velocity (μm/sec) of ER and cytosolic GFP measured by KbiFlow software.

Plant	Number of Cells	Maximal Velocities	S. D.	S. E.	Average Velocities	S. D.	S. E.
GFP-h							
Interior	16	2.196	0.709	0.177	0.482	0.173	0.043
Periphery	16	1.353	0.622	0.156	0.329	0.110	0.028
Cytosolic GFP							
Interior	22	1.989	0.755	0.161	0.493	0.199	0.043
Periphery	22	1.225	0.424	0.090	0.365	0.115	0.024
GFP-h	42	2.062	0.653	0.119	0.417	0.122	0.022
xik-1	29	0.757	0.345	0.064	0.219	0.099	0.018
xik-2	57	0.682	0.297	0.039	0.204	0.076	0.010
mya1-1	30	2.041	0.959	0.175	0.379	0.150	0.027
mya1-2	36	1.888	0.816	0.149	0.412	0.240	0.044
mya2-2	30	1.812	0.621	0.113	0.392	0.131	0.024
xik-2 mya1-1	30	0.503	0.259	0.047	0.143	0.050	0.009
xik-2 mya2-2	28	0.646	0.291	0.055	0.178	0.052	0.010
mya1-1 mya2-2	30	1.816	0.610	0.111	0.350	0.104	0.019
xik-2 mya1-1 mya2-2	34	0.394	0.196	0.034	0.118	0.030	0.005
xik-1 mya1-2 mya2-1	35	0.332	0.162	0.028	0.121	0.036	0.006